

# Prolate-to-oblate transition and backbending along the yrast line induced by quasiparticle alignment

Fang-Qi Chen<sup>1,\*</sup> and Q. B. Chen<sup>2</sup>

<sup>1</sup>*School of Physical Science and Technology, Northwestern Polytechnical University, Xi'an 710129, China*

<sup>2</sup>*Physik-Department, Technische Universität München, D-85747 Garching, Germany*

(Dated: July 14, 2020)

The yrast lines in Kr isotopes with  $N = 42, 44,$  and  $46$  are investigated in a beyond mean field framework with both prolate-oblate coexistence and quasiparticle alignment taken into account. Quasiparticle orbitals with high- $j$  and low- $\Omega$  on the oblate side are shown to be responsible for the sharp backbending observed in  $^{82}\text{Kr}$ , by driving the yrast shape from prolate to oblate. This suggests that quasiparticle alignment may not be neglected in the investigation of the shape evolution along the yrast line.

The Kr isotopic chain from the neutron-deficient to the neutron-rich side shows a rich collection of structure phenomena and has attracted experimental and theoretical interests over the years. Nuclear shape in the ground and low-lying states is one of the topics discussed intensively in this aspect. For example, coexisting  $0^+$  states with different deformations [1–3] and rapid shape transitions with increasing neutron numbers [4] and so on has been observed and understood in terms of various mean-field [5, 6] and beyond-mean-field [7–11] theories. In these theoretical studies it is noted that beyond-mean-field effects like symmetry restoration or mixing of different shapes can be important in understanding the remarkable phenomena observed [9].

Besides that along the isotopic chain, the shape evolution along the yrast line is another interesting aspect in the structure studies. In this case it demands a proper understanding for the high-spin region, in which the pair breaking due to the Coriolis effect, i.e., the quasiparticle alignment, may play an essential role. For example, lifetime measurements in  $^{74}\text{Kr}$  have found pronounced reduction of prolate deformation after the  $S$ -band crossing [12], which is described by the total Routhian surface (TRS) calculation.

The TRS calculation [13] which provides energy surfaces at specified rotational frequencies, is a powerful tool in revealing the shape evolution along the yrast line. However, as a mean field description the rotational symmetry remains broken, and the configuration mixing is not allowed in the TRS calculation. On the other hand, the projected shell model (PSM) [14, 15] is another powerful framework for the high-spin spectra, with the rotational symmetry restored and the configuration mixing taken into account. The PSM has been applied to high-spin studies of various deformed mass regions, including the Kr isotopes [16–20]. One of the greatest success of the PSM is the description of the backbending phenomenon induced by the quasiparticle alignment.

The backbending described by the PSM involves the breaking of pairs formed by quasiparticle orbitals with high- $j$  and low- $\Omega$  that are sensitive to the Coriolis effect. These aligned orbitals are defined at the deformation that is adopted for the ground state. This identity of deformations of the vacuum

and the multi-quasiparticle configurations results from the assumption of a fixed deformation parameter in the PSM, which is good for the well deformed nuclei, but not necessary for the transitional nuclei such as the Kr isotopes. Moreover, the fixed deformation assumed in the PSM leaves little room for the shape coexistence in the ground state, as well as the shape evolution with increasing spin.

As a generalization of the PSM, various deformations are taken into account in the framework proposed in Refs. [21, 22], in which HFB vacua of different deformations, as well as two-quasiparticle configurations based on each of them, are involved in the configuration space. Such a framework can be expected to provide a proper description to the transitional nuclei, in which the shape coexistence or shape evolution might exhibit.

In particular, with the allowance of various shapes a new manner of backbending might be anticipated. This kind of backbending involves the breaking of oblate pairs when the ground state is basically prolate. While the energy of the oblate vacuum increases quickly with spin, the corresponding aligned two-quasiparticle configuration can dive into the yrast region due to the strong Coriolis effect. Therefore, the backbending in this case takes place simultaneously with a prolate-to-oblate shape transition. Similar to the typical backbending described in traditional PSM calculations, the backbending here involves also high- $j$  and low- $\Omega$  orbitals, which locate near the top of a high- $j$  sub-shell in the oblate case. Therefore, this kind of backbending might happen when the Fermi level come close to the top of a high- $j$  sub-shell. This is in contrast to the typical backbending in the well deformed case, in which a Fermi level near the bottom of a high- $j$  sub-shell is expected. The existence of such backbending phenomenon originates from the opposite orders of members in a high- $j$  shell with prolate and oblate deformations. Note that the same character of Nilsson levels also leads to the existence of oblate high- $K$  isomers related to the  $\pi h_{11/2}$  shell as reported very recently [23].

In this paper the yrast lines of Kr isotopes with  $N = 42, 44,$  and  $46$  are studied within the framework proposed in Refs. [21, 22], in order to show the effect of oblate pair breaking on the yrast behavior.

The model framework adopted in this work has been presented in Ref. [21] and only a brief outline is given here. The Hamiltonian used in the model is of the pairing plus

arXiv:2007.06217v1 [nucl-th] 13 Jul 2020

---

\*Electronic address: fangqi0591@nwpu.edu.cn

quadrupole type [14]

$$\hat{H} = \hat{H}_0 - \frac{\chi}{2} \sum_{\mu} \hat{Q}_{\mu}^{\dagger} \hat{Q}_{\mu} - G_M \hat{P}^{\dagger} \hat{P} - G_Q \sum_{\mu} \hat{P}_{\mu}^{\dagger} \hat{P}_{\mu}, \quad (1)$$

which is diagonalized in a model space consists of a series of axially symmetric HFB vacua:

$$|\Phi(\beta)\rangle, \quad (2)$$

as well as two-quasiparticle states built on them:

$$\alpha_i^{\dagger}(\beta) \alpha_j^{\dagger}(\beta) |\Phi(\beta)\rangle. \quad (3)$$

The HFB vacua are determined by the variation

$$\delta \langle \Phi(\beta) | \hat{H} - \lambda_n \hat{N} - \lambda_p \hat{Z} - \lambda_q \hat{Q}_0 | \Phi(\beta) \rangle = 0, \quad (4)$$

with the constraint on particle numbers and quadrupole moments, while the quasiparticle operators  $\alpha_i(\beta)$  are defined as

$$\alpha_i(\beta) |\Phi(\beta)\rangle = 0. \quad (5)$$

Both of the vacua (2) and the two-quasiparticle configurations (3) are projected onto good angular momentum and particle numbers, so the ansatz for the wave function reads

$$|\Psi_{\sigma}^I\rangle = \sum_{\rho} f_{\sigma\rho}^I \hat{P}_{MK}^I \hat{P}^N \hat{P}^Z |\Phi_{\rho}\rangle, \quad (6)$$

with the index  $\rho$  running over the deformation  $\beta$  as well as the vacua and two-quasiparticle configurations  $\{i, j\}$  considered. The coefficients  $f_{\rho}^I$  are determined by solving the Hill-Wheeler equation

$$\sum_{\rho'} [\mathcal{H}^I(\rho, \rho') - E_{\sigma}^I \mathcal{N}^I(\rho, \rho')] f_{\sigma\rho'}^I = 0, \quad (7)$$

with the norm and energy overlaps defined as

$$\begin{aligned} \mathcal{N}^I(\rho, \rho') &\equiv \langle \Phi_{\rho} | \hat{P}_{KK'}^I \hat{P}^N \hat{P}^Z | \Phi_{\rho'} \rangle, \\ \mathcal{H}^I(\rho, \rho') &\equiv \langle \Phi_{\rho} | \hat{H} \hat{P}_{KK'}^I \hat{P}^N \hat{P}^Z | \Phi_{\rho'} \rangle. \end{aligned} \quad (8)$$

Note that the projected basis

$$\{\hat{P}_{MK}^I \hat{P}^N \hat{P}^Z | \Phi_{\rho}\rangle\} \quad (9)$$

is not orthogonal normalized [14] so the coefficients  $f_{\sigma\rho}^I$  can not be understood as the probability amplitude for the intrinsic configuration  $|\Phi_{\rho}\rangle$ . The probability amplitudes are defined as [26]

$$g_{\sigma}^I(\rho) = \sum_{\rho'} \Pi^{1/2}(\rho, \rho') f_{\sigma\rho'}^I \quad (10)$$

with  $\Pi^{1/2}(\rho, \rho')$  obtained by the diagonalization of the norm matrix (8):

$$\sum_{\rho'} \mathcal{N}_{\rho\rho'}^I u_{k\rho'}^I = n_k^I u_{k\rho}^I, \quad (11)$$

$$\Pi^{1/2}(\rho, \rho') = \sum_{\kappa} u_{k\rho}^I \sqrt{n_{\kappa}^I} u_{k\rho'}^{I*}. \quad (12)$$

Therefore,  $|g_{\sigma}^I(\rho)|^2$  are understood as the weight of the configuration  $|\Phi_{\rho}\rangle$  in the wave function (6) and satisfy the normalization condition as

$$\sum_{\rho} |g_{\sigma}^I(\rho)|^2 = 1. \quad (13)$$

In our calculations the neutron and proton major shells with  $N = 2, 3,$  and  $4$  are considered as the single-particle model space. The spherical single-particle energies for the single-particle part  $\hat{H}_0$  in (1) are determined by the Nilsson scheme at  $\beta = 0$ , with a modification for the Nilsson parameters  $\kappa$  and  $\mu$  taken from Ref. [24]. The  $\kappa$  and  $\mu$  for the neutron shell  $N = 4$  are multiplied by a factor 1.12 and those for the same proton shell are multiplied by 1.3. These modifications are done in order to obtain reasonable energy curves as noted in Ref. [21]. The strengths  $\chi$  of the quadrupole-quadrupole interactions are 90% of those in the earlier PSM calculation for  $^{78}\text{Kr}$  [19] and are kept constant for all of the isotopes studied. The monopole pairing strengths  $G_M$  also come from the earlier PSM calculations [16, 19], and the quadrupole pairing strength are  $G_Q = 0.16G_M$ . The energy cutoff for the intrinsic configurations  $|\Phi_{\rho}\rangle$  are the same as that in Ref. [21]. The effective charges in the  $B(E2)$  calculations are  $e^{\pi} = 1.35e$  for proton and  $e^{\nu} = 0.35e$  for neutron, adjusted to get an overall agreement with the observed transition strength  $B(E2, 2_1^+ \rightarrow 0_1^+)$ .

As a preparation for the following discussions, an overall impression of the mean field aspects of the Kr isotopes studied are given in Fig. 1. Fig. 1(a) shows the projected energy curves at  $I = 0$ . Two minima with prolate and oblate deformations can be found for all of the three isotopes. The prolate minimum in  $^{78}\text{Kr}$  locates at  $\beta \sim 0.33$ , in coincidence with the deformation parameter adopted in the earlier PSM calculation [19]. The oblate minimum lies about 1.5 MeV above the prolate one, suggesting the prolate dominance in the ground and low-spin states. The deformation of the prolate (absolute) minimum tends to decrease with the neutron number, in accordance with the increasing excitation energy observed for the  $2_1^+$  states [25]. It suggests that the neutron Fermi level locates in the upper half of the  $\nu g_{9/2}$  sub-shell, moving towards its top as the neutron number increases. In this case, the active  $g_{9/2}$  orbitals around the Fermi level are the high (low)- $\Omega$  ones for the prolate (oblate) side, as can be inferred from the Nilsson diagram for neutron shown in Fig. 1(b). Note that the location of the Fermi level and the prolate deformed ground state fulfill the requirements for a favored oblate quasiparticle alignment, as discussed above. Moreover, Fig. 1(a) show that the energy difference between the two minima gets lower as the neutron number increases, suggesting a growing importance of the oblate configurations.

The obtained yrast spectra are compared with the experimental ones [25] in Fig. 2 in terms of the so-called ‘‘back-bending plot’’, which gives the moment of inertia (MoI)

$$\mathfrak{J} = \frac{2I - 1}{E(I) - E(I - 2)} \quad (14)$$

as a function of the rotational frequency

$$\hbar\omega = \frac{E(I) - E(I - 2)}{2}. \quad (15)$$

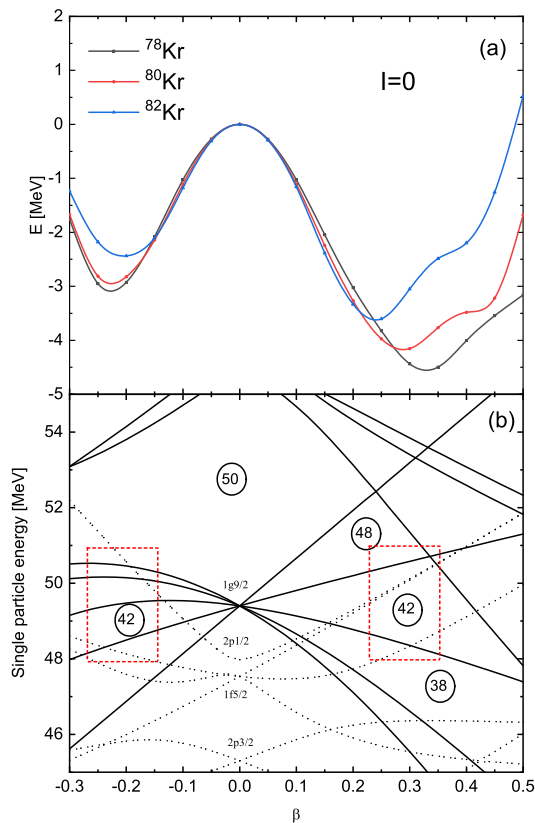


FIG. 1: (a) Projected energy curves at  $I = 0$  for  $^{78-82}\text{Kr}$ . The energies are normalized to  $\beta = 0$  in each curve. (b) Deformed neutron single-particle levels, calculated for  $^{82}\text{Kr}$  as an example. The solid (dashed) lines denote positive (negative) parity states. The Fermi level at the prolate/oblate minimum locates in the area circled by the dotted rectangles.

Such a plot is sensitive to the irregularities in the yrast band and is widely used in the studies of band crossing phenomena. The agreement between the experimental data and the calculated results is good. The problem with the MoI at  $I = 2$  found in the earlier PSM calculation [19] is now solved with the consideration of the oblate part. As the neutron number increases, the irregularities in the yrast bands take place earlier and become stronger, showing an enhanced tendency of pair breaking. This is in contrast to the shell filling pattern on the prolate side discussed above, as the high- $\Omega$   $\nu g_{9/2}$  orbitals around the Fermi level are less sensitive to the Coriolis effect. Therefore, the irregular behavior in the yrast bands shown in Fig. 2 indicates the possible existence of oblate pair breaking.

As another important observable, the calculated strength of the  $E2$  transitions along the yrast line are presented in Fig. 3, in comparison with the experimental data [25]. An overall agreement between the theoretical and the experimental results is achieved. For the low-spin part the decreasing trend of the  $B(E2)$  versus the neutron number is qualitatively reproduced, in line with the reduced tendency of deformation shown in Fig. 1(a). In  $^{78}\text{Kr}$  a dip of the  $B(E2)$  is found at around  $I = 10$ , where the irregularity in MoI emerges (see Fig. 2), as a reflection of some structures change taking place.

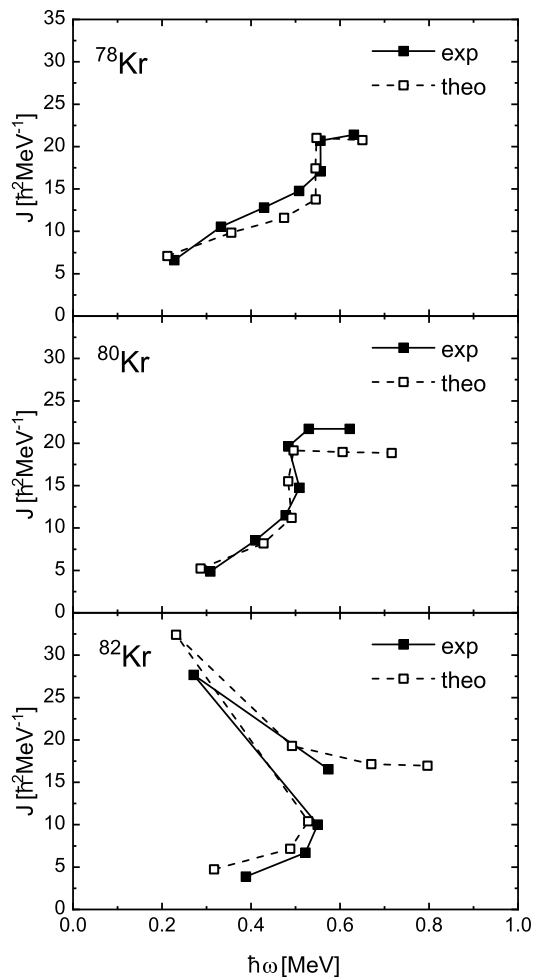


FIG. 2: The calculated moment of inertia as functions of the rotational frequency for the yrast bands in  $^{78-82}\text{Kr}$ , in comparisons with the experimental data taken from Ref. [25].

Such kind of dips get more pronounced in  $^{80}\text{Kr}$  and  $^{82}\text{Kr}$ , in accordance with the enhanced MoI irregularity, indicating abrupt structure change in these isotopes. In particular, the dip found in  $^{82}\text{Kr}$  is so pronounced that the  $B(E2)$  at  $I = 8$  is of only the order of 1 W.u.. Such a remarkable dip, together with the dramatic backbending shown in Fig. 2, suggests little interaction between the two crossing configurations, which are likely to have, therefore, very different structures.

The above discussions on the yrast spectra and  $E2$  transitions hint the appearance of oblate pair breaking and the consequent crossing between prolate and oblate configurations. The actual existence of these mechanisms can be illustrated in Fig. 4, in which the weight  $|g_{\sigma}^l(\rho)|^2$  of various types of configurations are presented as functions of spin. The total weight of the prolate deformed vacua are given in panel Fig. 4(a) for the three isotopes. For all of them the weight of the prolate vacua are close to 1 at low spins, in accordance with the prolate dominance shown in the energy curves (see Fig. 1(a)). The largest value is found in  $^{78}\text{Kr}$ , who has the largest energy difference between the prolate and oblate minima. The weight

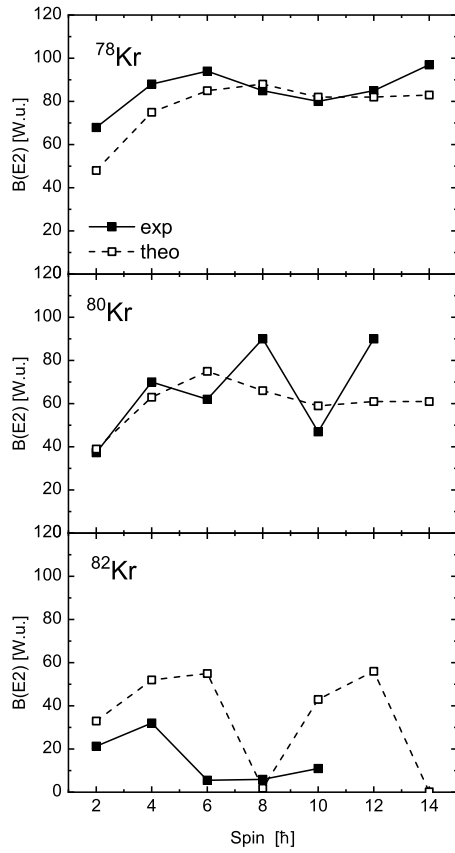


FIG. 3: The calculated  $B(E2)$  along the yrast lines in  $^{78-82}\text{Kr}$ , compared with the experimental data taken from Ref. [25].

of the prolate vacua decrease with spin, as a result of the band crossing. Note that the slope of the decreasing reaches maximum at the spin range where the irregularity in MoI takes place, due to the relatively rapid configuration change in the crossing region. The contributions from the prolate vacua become negligible after the band crossing.

The weight of the prolate two-quasiparticle configurations are given in Fig. 4(b). They are small at the beginning and increase smoothly before the band crossing. In this stage the prolate dominance remains in the yrast states and the increased weight here are contributed by the alignment of the prolate quasiparticles. As discussed above, this kind of alignment is moderate and does not lead to dramatic backbending in the MoI. In the band crossing region the behavior of the three isotopes become very different. For  $^{78}\text{Kr}$  the weight of the prolate two-quasiparticle configurations keeps increasing until the maximum value close to 1. This suggests that the irregularity (upbending) in the MoI of  $^{78}\text{Kr}$  can be related to the crossing of two prolate configurations (the vacuum and the two-quasiparticle configuration from  $\nu g_{9/2}$  orbitals), in consistent with the band crossing pattern provided in traditional PSM calculations. The weight of the prolate two-quasiparticle configurations for  $^{80}\text{Kr}$  stop increasing at the point of band crossing and keeps smaller than that for  $^{78}\text{Kr}$  afterwards. This behavior is inconsistent with the stronger MoI irregularity ob-

served in  $^{80}\text{Kr}$ , indicating ingredients other than the prolate quasiparticle alignment may play a role in this case. Finally for  $^{82}\text{Kr}$ , the weight of the prolate two-quasiparticle configurations experience dramatic decrease in the crossing region. Having little contribution from the prolate part, the yrast states right after the crossing point must be basically oblate. The sharp backbending observed in  $^{82}\text{Kr}$  is therefore induced by the crossing between the prolate and oblate configurations, which is likely to be abrupt due to the small overlap between the two. Furthermore, it seems that in  $^{82}\text{Kr}$  the prolate two-quasiparticle configurations become dominant again at  $I = 14$ , being consistent with the second drop of the theoretical  $B(E2)$  shown in Fig. 3. However, this is the result obtained without the consideration of four-quasiparticle configurations, which may play a role at such a high spin. Therefore, the interpretation of the  $I = 14$  member of the yrast band remains open and more experimental information is needed.

As the counterpart of panel Fig. 4(b), the weight of the oblate two-quasiparticle configurations are shown in Fig. 4(d). The large bump at the crossing region shown for  $^{82}\text{Kr}$  confirms the oblate nature of the yrast states in the range  $I = 8-12$ , supporting the prolate-to-oblate transition proposed above. A smaller bump is found for  $^{80}\text{Kr}$  in the same spin range, showing the oblate contribution, coexisting with the prolate part, that is responsible for the upbending behavior. For  $^{78}\text{Kr}$  the oblate two-quasiparticle configurations makes no contribution, in consistent with the traditional band crossing pattern suggested.

In contrast to the oblate two-quasiparticle configurations, the oblate vacua make little contribution to the yrast bands in the whole spin range investigated, as shown in Fig. 4(c). The weight around 0.2 at  $I = 0$  drops quickly with spin and becomes almost vanish before the crossing region. This is in accordance with the well known fact that the rotated oblate minima is disfavored compared with the prolate ones, as can be seen in Fig. 8(a) of Ref. [9], for instance.

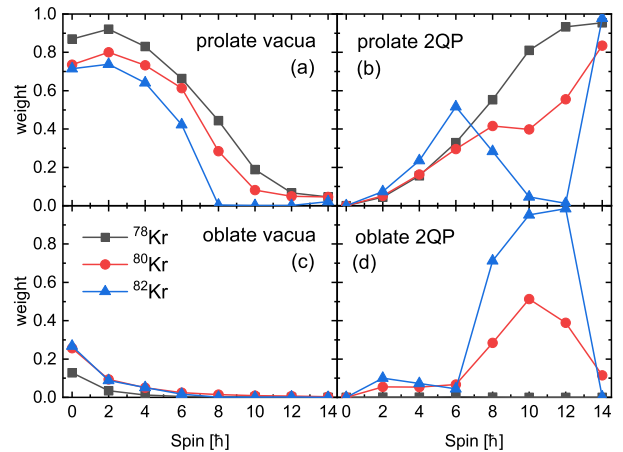


FIG. 4: Weight of various types of configurations calculated for the yrast bands in  $^{78-82}\text{Kr}$ : (a) prolate vacua; (b) prolate two-quasiparticle configurations; (c) oblate vacua; (d) oblate two-quasiparticle configurations.

For a better understanding of the yrast line behavior, quasi-

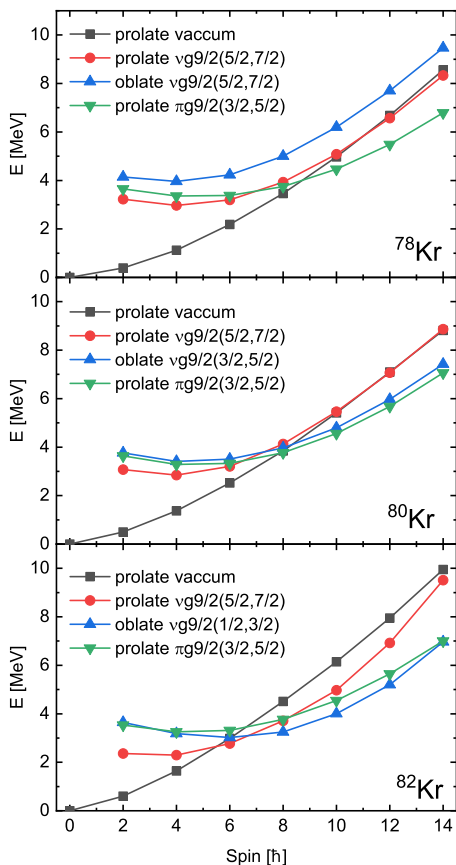


FIG. 5: The band diagrams defined as a generalization of those in PSM (see text) for  $^{78-82}\text{Kr}$ , with those configurations relevant in the yrast region included.

particle orbitals that are relevant to the crossing configurations need to be specified, as in the discussions on the traditional backbending phenomena. For this purpose one refers to the so-called “band diagram”, which is widely used in the PSM analysis [14]. A “band” in such a diagram is formed by projecting a specific intrinsic configuration (with the deformation fixed in the PSM) onto various spins, and the configuration corresponding to the lowest band is recognized as the dominant one for the yrast state. However, with the variation of deformation opened up in our framework, the concept of the band diagram has to be generalized. For example, the two-quasiparticle configuration  $\nu g_{9/2}(5/2, 7/2)$  (here 5/2 and 7/2 are the quantum numbers of the projection of the single particle angular momentum onto the three-axis of the intrinsic frame) can be built on a series of prolate vacua, with deformations  $\beta = 0.20, 0.25, 0.30$ , etc. Each of them can be projected, forming a subspace at each given spin in which the Hamiltonian can be diagonalized. The lowest energy obtained in such a diagonalization corresponds to the optimal combination of the above deformations, under the given configuration  $\nu g_{9/2}(5/2, 7/2)$ , and is thus defined as the “band energy” in the present case.

The band diagrams described above are presented in Fig. 5 for  $^{78-82}\text{Kr}$ , with those relevant configurations close to the

Fermi surfaces taken into account. The variation of the band crossing pattern from  $^{78}\text{Kr}$  to  $^{82}\text{Kr}$  can be found in this plot. For  $^{78}\text{Kr}$  the prolate  $g$ -band (projected from vacuum) is crossed by the prolate two-quasiparticle configuration  $\pi g_{9/2}(3/2, 5/2)$ , which is the  $\pi g_{9/2}$  configuration lying closest to the Fermi level. The lowest  $\nu g_{9/2}$  band on the prolate side, i.e.,  $\nu g_{9/2}(5/2, 7/2)$ , also cross the prolate  $g$ -band but at a higher energy. On the other hand, the lowest oblate band with the configuration  $\nu g_{9/2}(5/2, 7/2)$  appears at a relatively high energy, away from the yrast region in the spin range investigated. This is in accordance with the PSM-like band crossing pattern obtained in the discussions of Fig. 4. For  $^{80}\text{Kr}$  the configuration of the lowest oblate band becomes  $\nu g_{9/2}(3/2, 5/2)$ . Unlike the oblate band in  $^{78}\text{Kr}$ , it crosses the prolate  $g$ -band at around  $I = 8$ , almost simultaneously with the prolate  $S$ -band  $\pi g_{9/2}(3/2, 5/2)$ . This is again in agreement with the conclusion drawn from Fig. 4 that the upbending in  $^{80}\text{Kr}$  is induced by both prolate and oblate two-quasiparticle configurations. For  $^{82}\text{Kr}$ , the oblate band with the configuration  $\nu g_{9/2}(1/2, 3/2)$  crosses the prolate  $g$ -band at around  $I = 6$  and becomes the lowest one afterwards, in accordance with the oblate-dominated band crossing suggested in Fig. 4. In general, a growing importance of the oblate quasiparticle alignments in the band crossing region can be found from  $^{78}\text{Kr}$  to  $^{82}\text{Kr}$ , in both the band diagrams and the weight calculations.

Such a growing importance of the oblate quasiparticle alignments can be understood from two aspects: (1) the position of the Fermi level; (2) the energy difference between the prolate and oblate minima. As the neutron number increases, the neutron Fermi level moves toward the top of the  $\nu g_{9/2}$  sub-shell. With oblate deformations the quantum number  $\Omega$  of the orbitals around the Fermi level become smaller in this process, as can be seen from the variation of the oblate configurations adopted in the band diagrams for the three isotopes. Therefore, the response to the Coriolis effect of the oblate configurations gets enhanced and their band energies at higher spins are thus suppressed. Moreover, the energy difference between the two minima decrease from  $^{78}\text{Kr}$  to  $^{82}\text{Kr}$ , as shown in Fig. 1(a). This makes the oblate configurations energetically more favored as the neutron number increases and thus more likely to play a role in the yrast region. Both aspects contribute to the variation of the band crossing pattern shown in the band diagrams.

In summary, the yrast lines in Kr isotopes with  $N = 42, 44$ , and 46 are investigated in this work. The model space consists of axially deformed HFB vacua of both prolate and oblate shapes, as well as explicit two-quasiparticle configurations based on them. Such a model space accounts simultaneously for the shape mixture ranging from the prolate to oblate and the pair breaking induced by Coriolis interaction. The sharp backbending observed in  $^{82}\text{Kr}$  is interpreted by the crossing between the prolate dominated vacuum and an oblate two-quasiparticle state, involving high- $j$  and low- $\Omega$  orbitals and is thus sensitive to the Coriolis effect. The oblate quasiparticle alignment is also found to play a role in the upbending observed in  $^{80}\text{Kr}$ , while in  $^{78}\text{Kr}$  its effect is negligible. The variation of the importance of the oblate two-quasiparticle states in the band crossing region in these Kr isotopes is un-

derstood in terms of the location of the neutron Fermi levels as well as the energy difference between the prolate and oblate minima. The band crossing pattern revealed here shows that a prolate-to-oblate shape transition can be induced by the quasiparticle alignment, accompanied by the backbending, and it is thus suggested that two-quasiparticle configurations might be necessary in the investigations on the shape evolution along the yrast line.

### Acknowledgments

Inspiring and valuable suggestions from L. J. Wang are acknowledged. F. Q. Chen thanks her mother in law, G. X.

Guo, for taking care of her baby during the quarantine due to COVID-19, which allows her to finish this work. This work is partly supported by the National Natural Science Foundation for Young Scientists of China under Grant No. 11905172, the Fundamental Research Funds for the Central Universities under Grants No. G2019KY05105, and the Deutsche Forschungsgemeinschaft (DFG) and National Natural Science Foundation of China (NSFC) through funds provided by the Sino-German CRC 110 “Symmetries and the Emergence of Structure in QCD” (DFG Grant No. TRR110 and NSFC Grant No. 11621131001).

- 
- [1] R. B. Piercey et al., Phys. Rev. C **25**, 1941 (1982).
  - [2] C. Chandler et al., Phys. Rev. C **56**, R2924 (1997).
  - [3] E. Bouchez et al., Phys. Rev. Lett. **90**, 082502 (2003).
  - [4] A. Gade et al., Phys. Rev. Lett. **95**, 022502 (2005).
  - [5] H. Abusara, S. Ahmad, Phys. Rev. C **96**, 064303 (2017).
  - [6] J. Xiang, Z. P. Li, Z. X. Li, J. M. Yao, J. Meng, Nucl. Phys. A **873**, 1 (2012).
  - [7] M. Bender, P. Bonche, P.-H. Heenen Phys. Rev. C **74**, 024312 (2006).
  - [8] M. Girod, J.-P. Delaroche, A. Gorgen, A. Obertelli, Phys. Lett. B **676**, 39 (2009).
  - [9] Y. Fu, H. Mei, J. Xiang, Z. P. Li, J. M. Yao, J. Meng, Phys. Rev. C **87**, 054305 (2013).
  - [10] J. M. Yao, K. Hagino, Z. P. Li, J. Meng, P. Ring, Phys. Rev. C **89**, 054306 (2014).
  - [11] T. R. Rodríguez, Phys. Rev. C **90**, 034306 (2014).
  - [12] A. Algora et al., Phys. Rev. C **61**, 031303(R) (2000).
  - [13] W. Satuła, R. Wyss, P. Magierski, Nucl. Phys. A **578**, 45 (1994).
  - [14] K. Hara, Y. Sun, Int. J. Mod. Phys. E **4**, 637 (1995).
  - [15] Y. Sun, Phys. Scr. **91**, 043005 (2016).
  - [16] R. Palit, J. A. Sheikh, Y. Sun, H. C. Jain, Nucl. Phys. A **686**, 141 (2001).
  - [17] Y. Sun, J. A. Sheikh, Phys. Rev. C **64**, 031302(R) (2001).
  - [18] S. Verma, R. Devi, S. K. Khosa, Eur. Phys. J. A **30**, 531 (2006).
  - [19] Y. X. Liu, S. Y. Yu, C. W. Shen, Science China **58**, 012001 (2015).
  - [20] X. Y. Wu, S. K. Ghorui, L. J. Wang, K. Kaneko, Y. Sun, Nucl. Phys. A **957**, 208 (2017).
  - [21] F. Q. Chen, J. L. Egido, Phys. Rev. C **93**, 064313 (2016).
  - [22] F. Q. Chen, J. L. Egido, Phys. Rev. C **95**, 024307 (2017).
  - [23] C. Lizarazo et al., Phys. Rev. Lett. **124**, 222501 (2020).
  - [24] T. Bengtsson, I. Ragnarsson, Nucl. Phys. A **436**, 14 (1985).
  - [25] National Nuclear Data Center, Brookhaven National Laboratory, <https://www.nndc.bnl.gov/ensdf/>.
  - [26] P. Ring, P. Schuck, *The Nuclear Many-Body Problem* (Springer-Verlag, Berlin, 1980).